



# Modular reactor for *in situ* X-ray scattering, spectroscopy and ATR-IR studies of solvothermal nanoparticle synthesis

Sani Y. Harouna-Mayer,<sup>a,b,\*</sup> Melike Gumus Akcaalan,<sup>a,†</sup> Jagadesh Kopula Kesavan,<sup>a,b</sup> Tjark R. L. Groene,<sup>a</sup> Lars Klemeyer,<sup>a,b</sup> Sarah-Alexandra Hussak,<sup>a,c</sup> Lukas Grote,<sup>a</sup> Davide Derelli,<sup>a</sup> Francesco Caddeo,<sup>a</sup> Cecilia Zito,<sup>a,b</sup> Paul Stützle,<sup>a</sup> Dorota Speer,<sup>a</sup> Ann-Christin Dippel,<sup>c</sup> Blanka Detlefs,<sup>d</sup> Yannik Appiarius,<sup>e</sup> Axel Jacobi von Wangelin<sup>e</sup> and Dorota Koziej<sup>a,b,\*</sup>

Received 23 July 2025

Accepted 31 October 2025

Edited by K. Kvashnina, ESRF – The European Synchrotron, France

† These authors contributed equally to this work.

**Keywords:** reactor design; solvothermal synthesis; complementary *in situ* X-ray absorption spectroscopy and X-ray scattering; multimodal *in situ* infrared spectroscopy; colloidal nanostructure.

**Supporting information:** this article has supporting information at journals.iucr.org/s

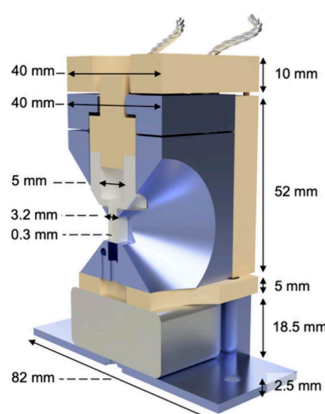
<sup>a</sup>University of Hamburg, Institute for Nanostructure and Solid-State Physics, Center for Hybrid Nanostructures (ChyN), Luruper Chaussee 149, 22761 Hamburg, Germany, <sup>b</sup>The Hamburg Center for Ultrafast Imaging, 22761 Hamburg, Germany, <sup>c</sup>Deutsches Elektronen Synchrotron DESY, Notkestraße 85, 22607 Hamburg, Germany, <sup>d</sup>ESRF – The European Synchrotron, 71 Avenue des Martyrs, CS40220, 38043 Grenoble, France, and <sup>e</sup>University of Hamburg, Department of Chemistry, Martin Luther King Platz 6, 20146 Hamburg, Germany. \*Correspondence e-mail: sani.harouna-mayer@uni-hamburg.de, dorota.koziej@uni-hamburg.de

Understanding the chemical processes that occur during the solvothermal synthesis of functional nanomaterials is essential for their rational design and optimization for specific applications. However, these processes remain poorly understood, primarily due to the limitations of conventional *ex situ* characterization techniques and the technical challenges associated with *in situ* studies, particularly the design and implementation of suitable reactors. Here, we present a versatile reactor suitable for *in situ* X-ray scattering, X-ray spectroscopy and infrared spectroscopy studies performed during solvothermal synthesis under autoclave-like, inert conditions. The reactor enables precise control of the temperature between  $-20^{\circ}\text{C}$  and  $200^{\circ}\text{C}$ , pressure up to 8 bar, magnetic stirring, and injection of gas or liquids. The reactor's capabilities are demonstrated by comprehensively studying the solvothermal synthesis of magnetite nanoparticles from iron acetylacetonate in benzyl alcohol through *in situ* X-ray scattering and spectroscopy, and attenuated total reflection infrared (ATR-IR) spectroscopy.

## 1. Introduction

Solvothermal synthesis is a versatile, fast, energy-efficient and scalable method for producing a wide range of materials in which chemical reactions between precursor(s) and solvent take place in a closed reaction vessel at elevated temperatures and pressures. Although it is widely used for synthesizing materials or composites, *e.g.* for electronic devices and energy conversion, the underlying reaction mechanisms that govern key properties such as crystallinity, particle size and morphology are often poorly understood (Heiligtag & Niederberger, 2013; Yin & Talapin, 2013; Boles *et al.*, 2016). In conventional laboratory experiments, the understanding of these mechanisms is typically limited to *ex situ* analysis of the final products or quenching the reaction at different reaction times. However, a deeper insight into these processes is crucial for the rational design of materials with tailor-made properties (Cansell & Aymonier, 2009; Deshmukh & Niederberger, 2017; Terraschke, 2023).

For this reason, solvothermal synthesis can be studied *in situ*, by using high-flux X-ray radiation from synchrotron light sources, allowing real-time monitoring of the reaction



and providing a comprehensive insight into the chemical steps involved (Jensen *et al.*, 2014; Bøjesen & Iversen, 2016). This approach requires specialized reaction vessels equipped with heating capabilities and additional features tailored to the specific reaction and technique being used. X-ray methods are particularly effective for *in situ* investigation of solvothermal synthesis as they provide valuable information about nucleation, growth and formation of intermediate states. For example, X-ray absorption spectroscopies (XAS) probe the electronic structure and the chemical environment of the absorbing atom (Koziej, 2016). Wide-angle X-ray scattering (WAXS) methods, such as powder X-ray diffraction (PXRD) and total scattering (TS), provide insights into the atomic structure while small-angle X-ray scattering (SAXS) enables the study of particle size, polydispersity, morphology and assembly (Broge *et al.*, 2020; Zhu *et al.*, 2021). A single technique cannot capture the full complexity of the reaction mechanisms across multiple length and time scales. It is rather the simultaneous application of different techniques in a multimodal or complementary approach that enables a more comprehensive understanding, *e.g.* by linking electronic, atomic and morphological evolution throughout the reaction (Grosso *et al.*, 2004; Andersen *et al.*, 2017; Grote *et al.*, 2021). However, each X-ray technique imposes distinct and often conflicting demands on the reactor design and specifications.

In order to meet these demands, several key challenges must be addressed when designing a tailor-made reactor for *in situ* X-ray studies:

(i) Window material. The material must be X-ray transparent at the required energies, chemically inert, and stable at elevated temperatures and pressures. It should also exhibit a low or easily subtractable background signal. Various materials are used depending on the technique and required reaction conditions:

(a) Polyimide is flexible, highly X-ray transparent and chemically inert, making it a common choice for both XAS and scattering experiments conducted under moderate conditions (Beyer *et al.*, 2014; Staniuk *et al.*, 2014; Thum *et al.*, 2024).

(b) Polyether ether ketone (PEEK) offers excellent X-ray transparency along with high chemical and mechanical stability, and is thus suitable for use at elevated temperatures and pressures. While it performs well in XAS setups, its semi-crystalline structure produces strong background signals, making it less suitable for scattering experiments (Grunwaldt *et al.*, 2005; Staniuk *et al.*, 2014; Klemeyer *et al.*, 2024).

(c) Fused silica is also chemically inert and can withstand high temperatures and pressures, but it offers somewhat lower mechanical stability and a slightly reduced X-ray transparency compared with PEEK. However, it has a low background signal for accurate background subtraction in scattering data. It is the commonly preferred window material for PXRD and TS experiments (Onur Şahin *et al.*, 2021; Roelsgaard *et al.*, 2023; Derelli *et al.*, 2024).

(d) Sapphire is suitable for the extreme temperatures and pressures of PXRD experiments. Its single-crystal reflections can be avoided by masking the detector or angular adjust-

ments. However, sapphire is not favorable for TS experiments due to its strong diffuse scattering signal (Chupas *et al.*, 2008; Becker *et al.*, 2010; Roelsgaard *et al.*, 2023).

(e) Beryllium is used in some experimental setups for its exceptional X-ray transparency and mechanical stability. However, its high toxicity necessitates strict safety protocols (Grunwaldt *et al.*, 2005; Bare *et al.*, 2007; Testemale & Brugger, 2024).

(ii) Geometry of the reactor and (iii) precise control over reaction parameters such as temperature, pressure, and (possibly) injection of reagents or gases to the chemical reactions inside the reactor. It is highly desirable to mimic the laboratory setups of preparative-scale chemical reactions, as variations in temperature or pressure profiles and sample volume can significantly influence the reaction mechanism and outcome. At the same time, the reactor must meet the space constraints of the beamline to allow *in situ* analytical experiments. Most *in situ* setups for X-ray scattering use capillaries, where small sample volumes are heated with hot air blowers or resistive heaters (Chupas *et al.*, 2008; Becker *et al.*, 2010; Roelsgaard *et al.*, 2023). This approach requires little space and allows rapid heating and good control over the reaction parameters. It can also be extended with gas or liquid injection devices. However, such a setup usually does not allow stirring of the reaction solution and the small volumes are usually not sufficient for post-synthesis analysis. Other setups use large reaction reservoirs from which small aliquots of the solution are circulated through a capillary for measurement, thereby mitigating beam damage (Yi *et al.*, 2015; Onur Şahin *et al.*, 2021). Bulky setups adapting commercial microwave reactors for the technical requirements of *in situ* measurements have also been reported (Tominaka *et al.*, 2018; Yamada *et al.*, 2019).

(iv) Safety of the beamline environment, especially when working at extreme conditions or with hazardous or toxic materials such as Be (Testemale & Brugger, 2024).

Table 1 summarizes selected literature reports on reactors enabling *in situ* analysis by XAS, WAXS and SAXS.

In an effort to address the aforementioned diverse requirements of a modular and versatile reactor, we developed a tailor-made setup for complementary experiments at synchrotron facilities. The reactor is compatible with a wide range of X-ray techniques, including XAS, PXRD, TS and SAXS, and supports solvothermal synthesis under inert, autoclave-like conditions. By exchanging the reactor inlet, the setup can be tailored for XAS experiments using a PEEK inlet or for scattering using glass inlets with various wall thicknesses – balancing background contribution and pressure resistance up to 8 bar. The system allows magnetic stirring and precise control of the heating ramp rate and reaction temperatures up to 200°C or cooling to –20°C via Peltier elements. Additional inlet modifications also support gas or liquid injection and integration of a fiber-optic attenuated total reflection (ATR) probe for simultaneous ATR infrared spectroscopy (ATR-IR) measurements. The reactor achieves sub-minute time resolution for *in situ* XAS and ATR-IR, and 1 s resolution for X-ray scattering experiments.

**Table 1**

Overview of reactors suitable for *in situ* XAS, WAXS and SAXS measurements during solvothermal synthesis.

The sample volume is categorized as small (*e.g.* capillary-based setups), medium (*e.g.* reactors with inlets) or large (*e.g.* flow reactors with external reservoirs). The classification reflects the typical sample quantity accessible for reaction monitoring or postmortem analysis. The '+' in the temperature column indicates the temperature employed in the respective study, rather than the maximum operational temperature, which was not specified in the respective report.

Reference	Methods	$T_{\max}$ (°C)	$p_{\max}$ (bar)	Window material	Wall thickness (mm)	Sample volume	Stirring
Evans <i>et al.</i> (1995)	WAXS	230	28	Steel	2.0	Medium	Yes
Grunwaldt <i>et al.</i> (2005)	XAS	200	250	PEEK, Be	1.0, 0.5	Medium	Yes
Bare <i>et al.</i> (2007)	XAS	600	14	Be	0.75	Small	No
Chupas <i>et al.</i> (2008)	WAXS, SAXS	1000	138	Al <sub>2</sub> O <sub>3</sub> , SiO <sub>2</sub> , polyimide	–	Small	No
Fingland <i>et al.</i> (2009)	XAS	400	3.5	Polyimide	0.3–1.2		No
		300	40	SiO <sub>2</sub>			
Becker <i>et al.</i> (2010)	WAXS, SAXS	450	400	Al <sub>2</sub> O <sub>3</sub> , SiO <sub>2</sub>	0.06–0.8	Small	No
van Beek <i>et al.</i> (2011)	WAXS	450+	20	SiO <sub>2</sub>	0.01	Small	No
Schaefer <i>et al.</i> (2011)	WAXS	225	207	Be	–	Medium	No
Borkiewicz <i>et al.</i> (2012)	WAXS, SAXS, XAS	48	–	Glassy carbon	–		No
Staniuk <i>et al.</i> (2014)	WAXS, XAS	180+	–	PEEK	0.5	Medium	No
Yi <i>et al.</i> (2015)	SAXS	–	–	SiO <sub>2</sub>	0.01	Large	Yes
Heidenreich <i>et al.</i> (2017)	WAXS, XAS	180	–	SiO <sub>2</sub> , Al	1.0–1.5, 0.1	Medium	No
Yao <i>et al.</i> (2017)	WAXS, XAS, IR	350	–	PTFE	–	Large	Yes
Hoffman <i>et al.</i> (2018)	WAXS	1000	35	SiO <sub>2</sub>	>0.1	Small	No
Kalantzopoulos <i>et al.</i> (2018)	WAXS	700+	–	SiO <sub>2</sub>	–		No
	WAXS	160+	–	SiO <sub>2</sub>	–	Medium	Yes
Onur Şahin <i>et al.</i> (2021)	WAXS	700+	–	SiO <sub>2</sub>	0.05	Large	Yes
Wang <i>et al.</i> (2022)	WAXS, SAXS, XAS	327	40	SiO <sub>2</sub>	0.2	Small	No
Prinz <i>et al.</i> (2023)	WAXS	500+	–	SiO <sub>2</sub>	0.02	Small	No
Testemale <i>et al.</i> (2024)	XAS	1200	2000	Glassy carbon, Be	–	Large	No
This work	WAXS, SAXS, XAS, ATR-IR	200	8	SiO <sub>2</sub> , PEEK	0.2–0.5	Medium	Yes

This reactor has already been employed in several studies investigating the solvothermal synthesis of alloy (Derelli *et al.*, 2024), metal oxide (Grote *et al.*, 2021), metal sulfide (Klemeyer *et al.*, 2024, 2025) and metal nitride (Harouna-Mayer *et al.*, 2025) nanoparticles. In these studies, we leveraged the reactor’s modular design and versatility across different X-ray techniques – exploiting, for instance, its low-background configuration for precise tracking of precursor conversion (Derelli *et al.*, 2024), its autoclave-like properties for spatially resolved synthesis at liquid–liquid interfaces at elevated pressure and temperature (Klemeyer *et al.*, 2025), and its air-tight conditions for sensitive materials (Harouna-Mayer *et al.*, 2025). Table S1 in the supporting information summarizes all the previous reactor designs. Here, we further demonstrate the reactor’s versatility by investigating as model system the partial reduction reaction of iron(III) acetylacetonate to Fe<sub>3</sub>O<sub>4</sub> magnetite nanoparticles in benzyl alcohol at 180°C (Pinna *et al.*, 2005), using *in situ* PXRD, TS, XAS and ATR-IR. Moreover, we also added cooling and injection capability to the cell, broadening its application range.

## 2. Reactor design

The reactor setup features a compact and user-friendly design optimized for safe operation. The assembled cross-sectional illustration of the reactor, including all dimensions, is shown in Fig. 1(a). For a comprehensive understanding of the system’s operating principle, it is beneficial to focus on the main

elements individually. The detailed representation of the assembly is given in Fig. 1(b). The reactor can be divided into three main components, *i.e.* the housing, the inlet, and the insulators.

The back and front center pieces were carved out of the aluminium housing in a conical shape to achieve an opening angle of 45° enabling data acquisition in transmission geometry, *e.g.* for high-*q* TS data, or in reflection geometry, *e.g.* high-energy-resolution fluorescence-detected XAS (HERFD-XAS). Fig. S1 of the supporting information shows a schematic of the reactor including the X-ray beam path for transmission geometry, *e.g.* for scattering experiments, and for reflection geometry, *e.g.* for HERFD-XAS experiments. The opening angle of 45° corresponds to a maximum instrumentally accessible *q* value of  $q_{\max, \text{inst}} = 38 \text{ \AA}^{-1}$  for an X-ray energy of 100 keV.  $q_{\max, \text{inst}}$  values depend on the X-ray energy as well as the instrumental setup including the opening angle of the reactor or sample environment, and the detector size and position. The corresponding  $q_{\max, \text{inst}}$  values for different X-ray energies and sample-to-detector distances are summarized in Table S2. Heating elements are vital for the thermal performance of the reactor setup, as they influence the heating of the aluminium housing, the inlet and the reaction solution. These factors determine the heating rate, final temperature and temperature stability. They surround the inlet and are driven with a 24 V–50 W power supply (EA-PS 5040, Elektro-Automatik) in parallel connection. The generated dielectric heating is distributed across the area that surrounds the inlet, evenly

via the thermal conductivity of the aluminium. The temperature is measured by a PT1000 model sensor (Honeywell) positioned close to the inlet and connected to an LS335 LakeShore temperature controller. The measured temperature is instantly read from the temperature controller to a computer and monitored via a Python script.

The inlet works as a custom-made container for the reaction solution accommodation. It is used with a cap and a perfluoro elastomer (FFKM) O-ring to provide an air-tight environment. The inlet design offers two material options: PEEK (Bieglo) and glass. The material is selected according to the measurement technique, and the X-ray window wall thickness can be adapted to the reaction requirements. PEEK is a favorable material for spectroscopy measurements due to its high X-ray transparency. Glass material is preferred for scattering experiments due to its low background signal although its utilization presents challenges regarding mechanical stability. In careful tests, we observed that determination of the optimum glass thickness as a balance between satisfactory data collection and structural integrity at high-pressure conditions is quite challenging. To this end, we designed glass and PEEK inlets with 0.2, 0.3 and 0.5 mm wall thicknesses. The results demonstrate that 0.2 mm thickness of the PEEK inlet and 0.3 mm thickness of the glass inlet gave the most satisfactory data for the spectroscopy and scattering experiments at relatively high pressures, respectively. Fig. 1(c) shows the various inlet and cap configurations for specific X-ray techniques and experimental requirements, with total and scan zone volumes, which are as follows:

(i) Glass inlet for scattering experiments under air-tight, autoclave-like conditions at elevated temperatures and pressures with a wall thickness of 0.3 mm.

(ii) Thin-walled (0.05 mm) glass vial embedded in a copper body for weak background scattering contributions. The corresponding PEEK cap features a spring, which prevents the fragile thin-walled glass vial from breaking upon closure and provides a modest degree of sealing, though not fully air-tight as in the standard glass inlet (i).

(iii) PEEK inlet for XAS measurements with a wall thickness of 0.2 mm.

(iv) A modified hollow-screwed PEEK cap that enables the pressure sensor to measure pressure from a position close to the solution.

(v) A modified hollow brass cap allowing the injection of reagents during the experiment through a septum.

(vi) A modified hollow brass cap for a fiber-optical ATR-IR probe implementation, enabling multimodal ATR-IR measurements.

Since boron silicate glass has a stable pH range of approximately 2–9, and PEEK can withstand pH values between 2 and 12, the inlets can also be used for hydrothermal synthesis within these respective pH ranges. However, this paper focuses on solvothermal synthesis; therefore, the pH stability of the inlets is beyond its scope.

Further details about the reactor tailored for cooling, photographs of the caps designated for pressure and IR measurements are given in the supporting information. A PEEK inlet can be used for X-ray scattering; however, due

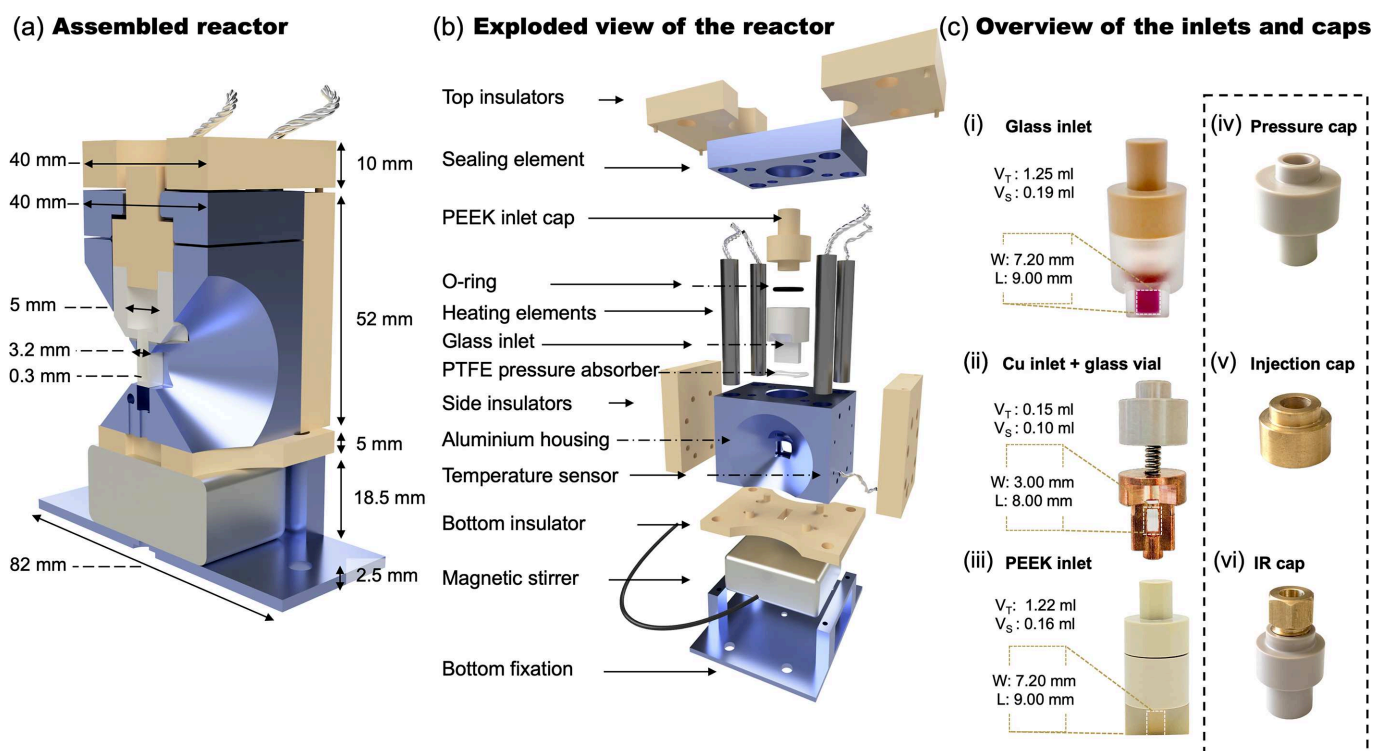


**Figure 1**

Design of the reactor. (a) Cross-sectional rendering of the assembled reactor. (b) Exploded schematic showing individual components. (c) Photograph of the interchangeable inlet modules for different experimental configurations,  $V_T$  and  $V_S$  indicate total volume and scanning area volume, respectively. W and L are the width and length of the scanning area.

to its polycrystalline nature, it introduces high residual background scattering. This trade-off is acceptable for strongly scattering crystalline samples, where the sample scattering intensity is sufficient to outweigh the residual background from PEEK (Staniuk *et al.*, 2014).

The insulation and the sealing elements complete the airtight environment, working as the supportive components. A tightly fastened aluminium component, mounted on top of the aluminium housing, ensures complete sealing of the reactor. Top, bottom and side PEEK insulators enhance the heat retention within the system by minimizing thermal exchange between the aluminium and surrounding air as much as possible. Properties such as high thermal stability, low thermal expansion coefficient, dimensional stability and low thermal conductivity, which make PEEK a perfect thermal insulator, support all the thermal requirements of the closed system.

To ensure a homogeneous colloidal dispersion, a microstirrer (Variomag Thermo Scientific) is installed on the aluminium bottom plate directly beneath the aluminium housing. A micromagnetic stirring bar is located within the inlet, providing homogeneous mixing of the solution during the *in situ* measurements. This ensures a constant concentration of the scatterers across the cell and high data quality.

### 3. Performance of the reactor

We demonstrate the performance and versatility of the reactor through a series of characterization and reaction studies. First, we evaluate its thermal response, pressure stability, and X-ray transparency (Fig. 2). We then estimate the signal-to-noise ratio of the PXRD pattern of nanoparticle dispersions at

different particle concentrations (Fig. 3). Finally, we investigate the model system, the solvothermal synthesis of magnetite nanoparticles, in detail using a combination of complementary *in situ* techniques: PXRD and pair distribution function (PDF) analysis of TS data (Fig. 4), ATR-IR (Fig. 5), and HERFD-XAS (Fig. 6). By combining all analytical data from these methods, we propose a reaction mechanism of the nanoparticle formation and postulate intermediate states during the transformation of iron(III) acetylacetonate,  $\text{Fe}(\text{acac})_3$ , to magnetite,  $\text{Fe}_3\text{O}_4$ , in benzyl alcohol (Pinna *et al.*, 2005). These results highlight the reactor's capability to integrate multiple methods, providing a comprehensive understanding of complex reaction pathways.

Fig. 2(b) shows photographs of the glass inlet during the  $\text{Fe}_3\text{O}_4$  nanoparticle synthesis. The color change of the reaction solution from reddish  $\text{Fe}(\text{acac})_3$  in benzyl alcohol (BnOH) to black  $\text{Fe}_3\text{O}_4$  is clearly visible during the heating ramp to  $180^\circ\text{C}$ . Fig. 2(c) depicts an IR image of the reactor window, illustrating uniform heat distribution in the BnOH-filled inlet at  $180^\circ\text{C}$ . We further measure the temperature and pressure profiles during heating: the BnOH-filled inlet reaches 3.8 bar at  $180^\circ\text{C}$ , while the water-filled inlet reaches 7.9 bar at  $150^\circ\text{C}$ , both without breaking the glass inlet with a 0.3 mm wall thickness, as shown in Fig. 2(d). To assess the suitability of the glass inlet for X-ray experiments, we calculate its X-ray transmission both empty and filled with the common solvents water, ethanol and BnOH. The results indicate reasonable transmission for X-ray energies above 20 keV, as shown in Fig. 2(e). For comparison, Fig. S6 shows the X-ray transmission of glass and PEEK inlets with different wall thicknesses,

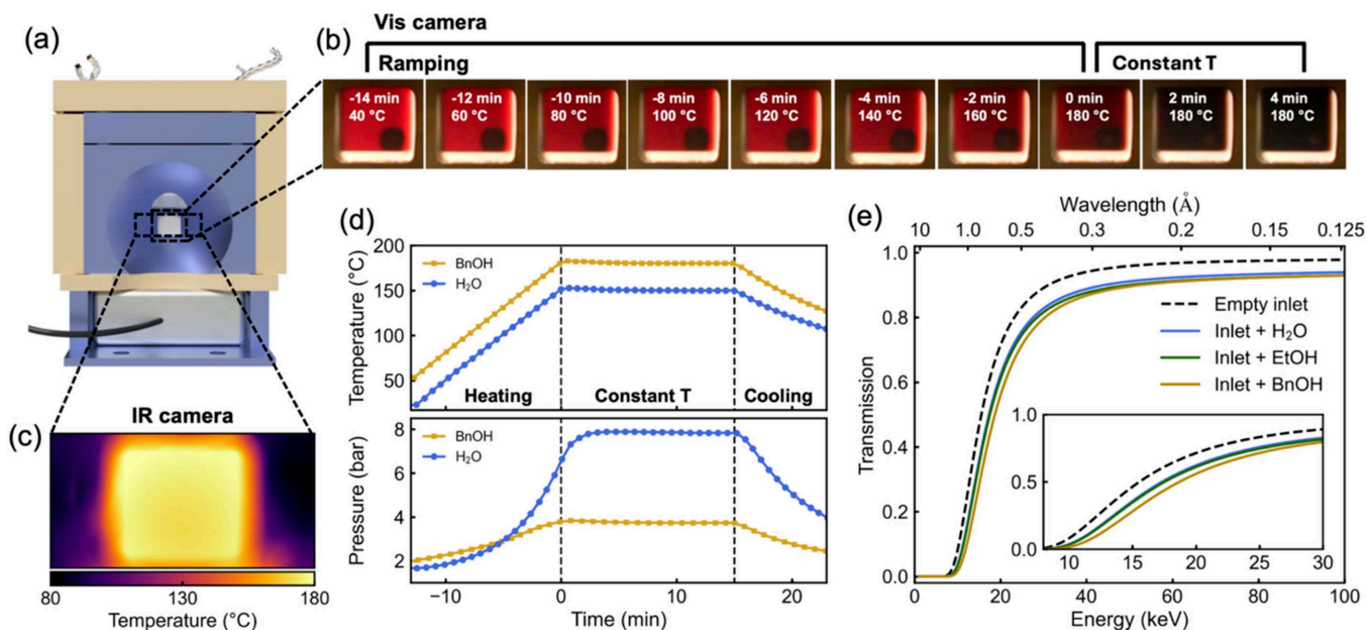


**Figure 2** Thermal, pressure, and transmission characteristics of the glass inlet with 0.3 mm wall thickness. (a) Front view rendered image of the reactor. (b) Photographs showing the solution color change during  $\text{Fe}_3\text{O}_4$  formation from  $\text{Fe}(\text{acac})_3$  in BnOH upon heating. (c) IR image showing uniform heat distribution of the BnOH-filled inlet at  $180^\circ\text{C}$ . (d) Temperature and pressure profiles during the heating of water and BnOH to  $150^\circ\text{C}$  and  $180^\circ\text{C}$ , respectively. (e) Simulated X-ray transmission of the inlet, empty and filled with the solvents water, ethanol (EtOH), and BnOH as a function of the X-ray energy.

providing guidelines for selecting suitable inlets. Details on the transmission calculations are given in the *Experimental* section.

The glass inlet configuration offers good pressure stability and air-tightness, enabling solvothermal synthesis under autoclave-like conditions for *in situ* scattering experiments. However, the relatively thick inlet walls give rise to a substantial scattering background. One major challenge of *in situ* scattering studies is the strong background signal, as scattering arises from all components in the beam path. To isolate the signal of the chemical species of interest, contributions from the solvent, reactor walls and beamline environment must be carefully subtracted. In most PXRD experiments, background subtraction is relatively straightforward due to the strong diffraction signal of crystalline phases. However, for weakly scattering systems such as nanoparticles or dilute dispersions or solutions, background subtraction becomes significantly more demanding. This is especially true for TS experiments, where often non-periodic structures or small nanoparticles are being investigated and data collected at high scattering vectors (typically  $q_{\max} > 15 \text{ \AA}^{-1}$ ), where scattering is weak and noisy. Moreover, standard baseline correction methods are not applicable in TS experiments, as both Bragg and diffuse scattering must be preserved, making accurate and precise background subtraction essential. Fig. 3(a) illustrates this by comparing PXRD patterns of commercial copper(II) oxide (CuO) nanoparticles (7.4 nm diameter) at concentrations of 0.2, 0.05 and 0.02 mmol ml<sup>-1</sup> in ethanol, highlighting the dominant background relative to

the nanoparticle signal. Additionally, we estimate the signal-to-noise ratio (SNR) for each concentration [Figs. 3(b)–3(e)], demonstrating that the reactor with glass inlets can still provide reasonable PXRD data even at very low particle concentrations.

We further test the reactor by studying the solvothermal synthesis of Fe<sub>3</sub>O<sub>4</sub> from Fe(acac)<sub>3</sub> in BnOH at 180°C (Pinna *et al.*, 2005). This reaction is fast, scalable, and allows tailoring of the size, morphology, and even synthesis of heterostructures (Kim *et al.*, 2009; Fantechi *et al.*, 2017; Nobile & Cozzoli, 2022). The organic reaction pathways during the synthesis of metal oxides in benzyl alcohol, including Fe<sub>3</sub>O<sub>4</sub>, are well known and have been assessed in previous studies via gas chromatography–mass spectrometry (GC-MS) and nuclear magnetic resonance (NMR) analysis of the final reaction mixture. In particular, it has been proposed that benzyl acetate and 4-phenyl-2-butanone form via the reaction of benzyl alcohol with Fe(acac)<sub>3</sub>. Furthermore, during the reaction, one third of Fe(III) species are reduced to Fe(II) by dehydrogenative oxidation of 4-phenyl-2-butanone into 4-phenyl-3-buten-2-one. The complete organic transformation pathway has been reported by Niederberger & Garnweitner (2006). However, *in situ* studies providing mechanistic insights that focus on the metal center, *e.g.* formation of intermediate complexes and monitoring the nucleation and growth of the nanoparticles, are scarce (Mikhailova *et al.*, 2022).

Based on our *in situ* scattering data, we propose a reaction mechanism, schematically illustrated in Fig. 4(a). Initially, Fe(acac)<sub>3</sub> is dissolved in BnOH with the Fe(III) center octa-

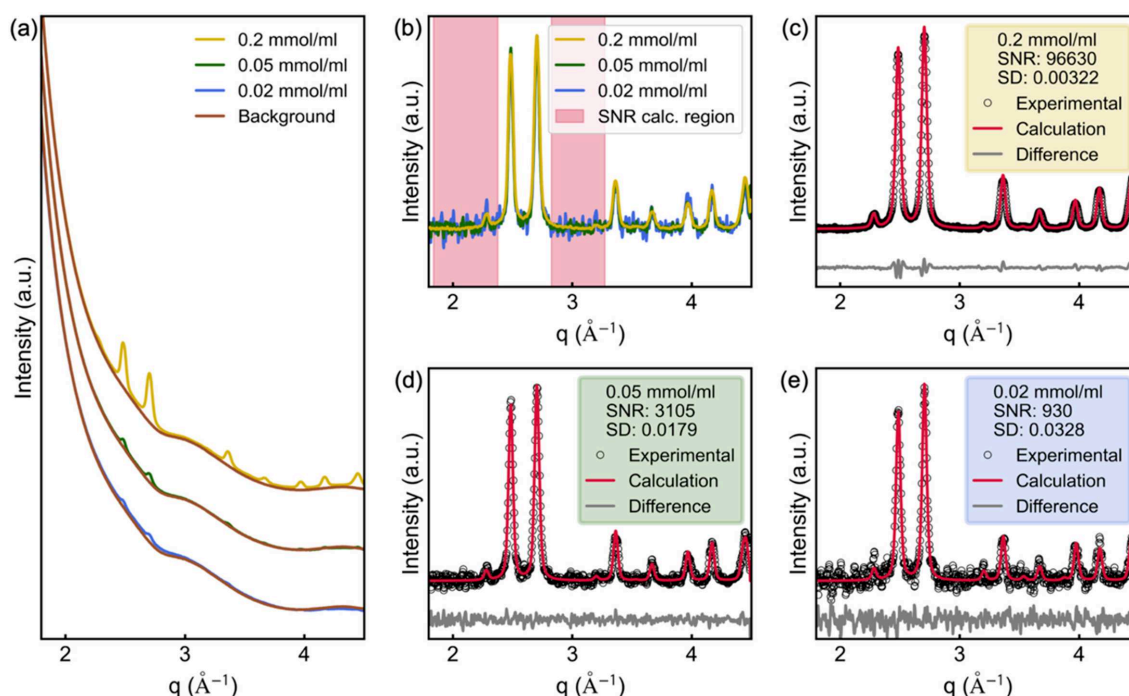


**Figure 3** PXRD of CuO nanoparticles (7.4 nm diameter) dispersed in ethanol at concentrations of 0.2, 0.05 and 0.02 mmol ml<sup>-1</sup> and signal-to-noise ratio (SNR) estimations. (a) PXRD of the CuO dispersions compared with the background pattern which is the ethanol-filled inlet. (b) Overlay of background-subtracted and normalized PXRD patterns for CuO dispersions showing increasing noise with decreasing concentration. (c–e) Rietveld refinements for each concentration. To estimate the SNR, we first normalize each pattern to 1 at the most intense Bragg peak ( $\sim 2.7 \text{ \AA}^{-1}$ ). The SNR is then calculated as the inverse square of the standard deviation (SD) of the difference between the experimental data and the Rietveld fit. To avoid influence from imperfections in the fit, regions containing strong Bragg reflections are excluded from the SD calculation as highlighted in (b).

hedrally coordinated by three acetylacetonate ligands, each coordinating through both oxygen atoms. Upon reaching 180°C, an intermediate ferric acetate complex,  $[\text{Fe}_3(\mu_3\text{-O})(\text{AcOR})_6(\text{ROH})_3]^+$ , forms. In this complex, three Fe(III) centers are linked to a central coplanar  $\mu_3$ -oxo ligand. Acetate groups (AcOR) bridge pairs of Fe(III) centers and are further coordinated by water or alcohol molecules (ROH), maintaining an octahedral coordination. Here, *R* denotes either a hydrogen atom or a benzyl group. The iron complex with coordinated acetate and water is well known in the literature (Anson *et al.*, 1997). With continued heating, the intermediate transforms into crystalline  $\text{Fe}_3\text{O}_4$  nanoparticles.

Figs. 4(b), 4(c) show the temperature profiles and heatmaps of the obtained *in situ* PXRD patterns and PDFs, respectively. The reaction solution is ramped at  $10^\circ\text{C min}^{-1}$ , with the time point of 0 min defined as the moment when the reaction temperature of 180°C is reached. Both datasets clearly reflect the sequential transformation through the three structural stages depicted in Fig. 4(a). To illustrate the reaction kinetics, we calculate a Pearson correlation map of the *in situ* PXRD data. The resulting map (Fig. S7) visualizes the degree of similarity between the PXRD patterns at the different reaction times. The structural changes indicated by the two nodes along the diagonal in the Pearson correlation map point at two transitions: one shortly after 0 min and a second around 25 min. Figs. 4(d), 4(e) show representative PXRD and PDF patterns for the three reaction stages: the initial molecular

complex (bottom), the intermediate (middle) and the final  $\text{Fe}_3\text{O}_4$  product (top). Rietveld refinement of the PXRD pattern of the final product confirms the phase purity of  $\text{Fe}_3\text{O}_4$ . The non-crystalline nature of the initial and intermediate states excludes conventional PXRD refinement; however, their structures can be analyzed via PDF. The initial state is modeled using the structure of  $\text{Fe}(\text{acac})_3$  while the intermediate state at 5 min reaction time is best described using a three-phase refinement with  $\text{Fe}(\text{acac})_3$ ,  $[\text{Fe}_3(\mu_3\text{-O})(\text{AcOR})_6(\text{ROH})_3]^+$  and  $\text{Fe}_3\text{O}_4$  in a 1.00:0.92:0.70 scale ratio. Based on the reported  $\text{Fe}(\text{acac})_3$  decomposition mechanism in benzyl alcohol forming benzyl acetate (Niederberger & Garnweitner, 2006), we propose the actual intermediate is a ferric acetate complex coordinated with benzyl acetate and benzyl alcohol ligands. However, for the PDF refinement, we employ the literature-reported structure  $[\text{Fe}_3(\mu_3\text{-O})(\text{AcO})_6(\text{H}_2\text{O})_3]^+$ , which contains acetate and water ligands (Anson *et al.*, 1997). We note that PDF analysis cannot unambiguously distinguish between acetate and benzyl acetate ligands, or between coordinated water and benzyl alcohol, due to the prevalence of short-range interatomic correlations involving Fe and the surrounding BnOH solvent. Nevertheless, the excellent agreement between the modeled and experimental PDFs [Fig. 4(e)] strongly supports the structural assignment of the intermediate as a ferric acetate complex. The refined parameters of the Rietveld and PDF refinements are given in Tables S3 and S4, respectively.

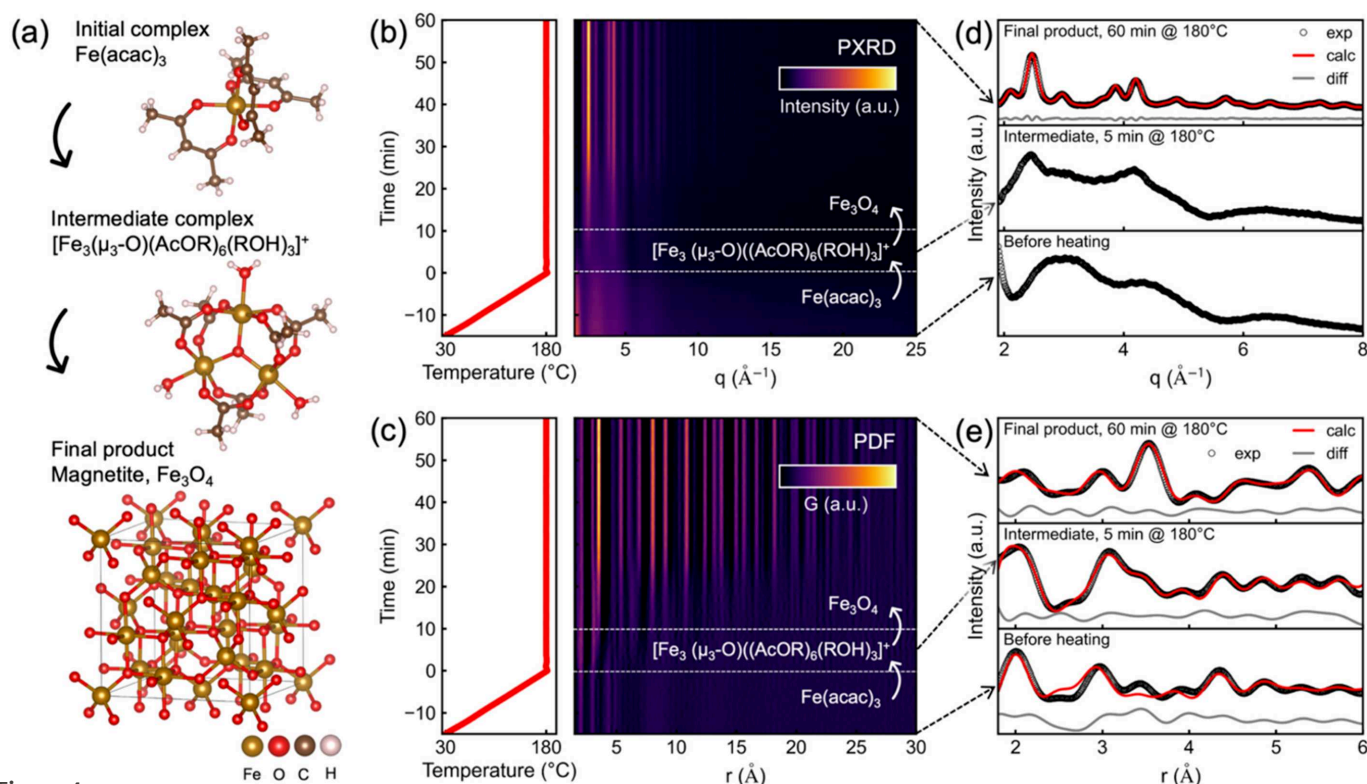


Figure 4

*In situ* PXRD and PDF analysis of the reaction to  $\text{Fe}_3\text{O}_4$ . (a) Schematic of the reaction mechanism as determined by PXRD and PDF refinements. The initial complex  $\text{Fe}(\text{acac})_3$  forms  $[\text{Fe}_3(\mu_3\text{-O})(\text{AcOR})_6(\text{ROH})_3]^+$  after reaching the reaction temperature of 180°C which further reacts to the final product  $\text{Fe}_3\text{O}_4$ . (b, c) Temperature profile and heatmap of PXRD and PDF data, respectively. (d, e) PXRD Rietveld and PDF refinements of the initial complex before heating,  $\text{Fe}(\text{acac})_3$ , the intermediate complex,  $[\text{Fe}_3(\mu_3\text{-O})(\text{AcOR})_6(\text{ROH})_3]^+$ , at 5 min after reaching the reaction temperature of 180°C and  $\text{Fe}_3\text{O}_4$ . Since Rietveld refinement requires a crystalline structure only the refinement of  $\text{Fe}_3\text{O}_4$  is shown for PXRD.

To assess the time resolution achievable with the reactor setup, Fig. S8 compares PXRD and PDF data averaged over varying exposure times. These tests demonstrate that high-quality data can be obtained with exposures as short as 5 s during the early, low-scattering stages of the reaction, and down to 1 s for the strongly scattering crystalline final product. Overall, these results highlight the capability of the reactor to provide high-quality PXRD and PDF data at low time resolution despite significant background scattering from the glass components.

The PDF refinement of the intermediate state assumes the thermal decomposition of acetylacetonate ligands into acetate. To track the formation of organic by-products in the liquid phase during the reaction, we perform *in situ* ATR Fourier transformed infrared (FTIR) spectroscopy using the reactor equipped with an ATR-IR fiber probe. *In situ* ATR-FTIR difference spectra collected during the reaction and reference spectra for comparison are displayed in Fig. 5. Already during the heating process, we observe a decrease in absorption in the frequency region around  $1000\text{ cm}^{-1}$ , which we assign to the  $\nu(\text{C-O})$  stretching vibration of BnOH. Furthermore, we observe a decrease in absorption around  $1600\text{ cm}^{-1}$ , which we attribute to the bending vibration  $\delta(\text{H-O-H})$  of residual water present in the sample at ambient conditions. As the temperature increases, this water evaporates and transitions into the gas phase, leaving the liquid phase and thus causing the observed signal loss. With further heating, a broadening and increase in absorption are seen around  $1225\text{ cm}^{-1}$ , which we assign to the emergence of  $\nu(\text{C-O})$  vibrations characteristic of an acetate functional group. We correlate this increase with the formation of benzyl acetate, supported by additional vibrational modes around  $1739\text{ cm}^{-1}$  [ $\nu(\text{C=O})$ ],  $1026\text{ cm}^{-1}$  and the symmetric and asymmetric bending vibrations [ $\delta(\text{CH}_3)$ ] at  $1361$  and  $1380\text{ cm}^{-1}$ , respectively. These obser-

vations are consistent with the reported formation of acetates during acetylacetonate decomposition (Mikhailova *et al.*, 2022). In addition to vibrational modes attributed to benzyl acetate formation, we also identify a vibrational mode at  $1717\text{ cm}^{-1}$  [ $\nu(\text{C=O})$ ], due to the contribution of acetone in the reaction mixture, which is formed alongside benzyl acetate. The assigned vibrational modes are listed in Table S5. For comparison, additional reference spectra are shown in Fig. S9. These ATR-FTIR findings for the synthesis of  $\text{Fe}_3\text{O}_4$  support the formation of a ferric acetate complex as an intermediate. They also demonstrate the capabilities of our reactor to acquire ATR-FTIR spectra with a spectral resolution of  $4\text{ cm}^{-1}$  and a temporal resolution of less than 1 min during solvothermal synthesis.

Finally, we investigate the  $\text{Fe}_3\text{O}_4$  solvothermal synthesis using XAS with the PEEK inlet configuration. Fig. 6(a) presents Fe *K*-edge HERFD-XANES spectra, showing a shift of the absorption edge to lower energy – indicating a partial reduction of  $\text{Fe}^{3+}$  in the initial and intermediate complexes to a mixed-valence  $\text{Fe}^{2+}/\text{Fe}^{3+}$  state in  $\text{Fe}_3\text{O}_4$ . Concurrently, the white-line double peak observed in the initial state transitions into a single, broader feature in the final product, while the pre-edge intensity increases, indicating changes in Fe coordination symmetry and oxidation state. These spectral features closely resemble previously reported XANES spectra of  $\text{Fe}(\text{acac})_3$  (Bauer *et al.*, 2005; Levish & Winterer, 2020) and  $\text{Fe}_3\text{O}_4$  (Okudera *et al.*, 2012; Piquer *et al.*, 2014), supporting the identification of the initial complex as  $\text{Fe}(\text{acac})_3$  and confirming the formation of  $\text{Fe}_3\text{O}_4$  as the final product.

To analyze these changes quantitatively, we perform multivariate curve resolution by alternating least-squares (MCR-ALS) (Jaumot *et al.*, 2005) of the *in situ* HERFD-XANES dataset, which extracts three distinct Fe species, consistent with the PDF findings. Fig. 6(b) shows the evolution of the three species during the reaction. Fig. 6(c) shows the MCR-ALS recovered spectra. In Fig. 6(d) we present results from *FEFF* simulations (Rehr *et al.*, 2010) based on the structures determined from the PDF analysis. Since  $\text{Fe}_3\text{O}_4$  contains Fe atoms in both octahedral and tetrahedral coordination sites in a 2:1 ratio, the simulation of  $\text{Fe}_3\text{O}_4$  was performed as a linear combination of *FEFF* simulated spectra calculated with Fe in octahedral and tetrahedral sites as the absorbing atom, weighted accordingly at a 2:1 ratio. The simulations match well with the MCR-ALS recovered spectra. Fig. S10 shows the *FEFF* simulated XANES spectra together with density-of-state (DOS) calculation of the Fe, O and C *s*, *p* and *d* states.

Overall, these results showcase the excellent performance of the reactor for *in situ* analyses such as high-resolution XAS and WAXS, as well as ATR-FTIR measurements, and demonstrate its capability to provide detailed electronic and structural insight during solvothermal synthesis.

#### 4. Conclusions

We present a versatile reactor system optimized for *in situ* X-ray scattering and X-ray absorption spectroscopy analysis

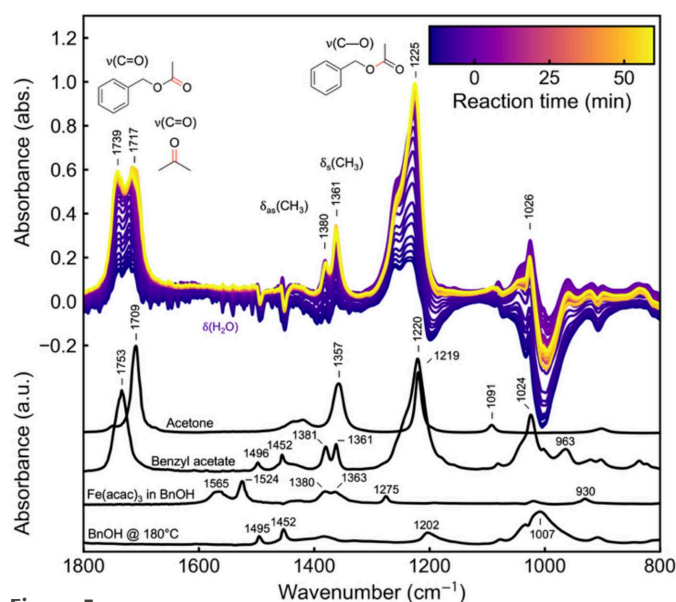
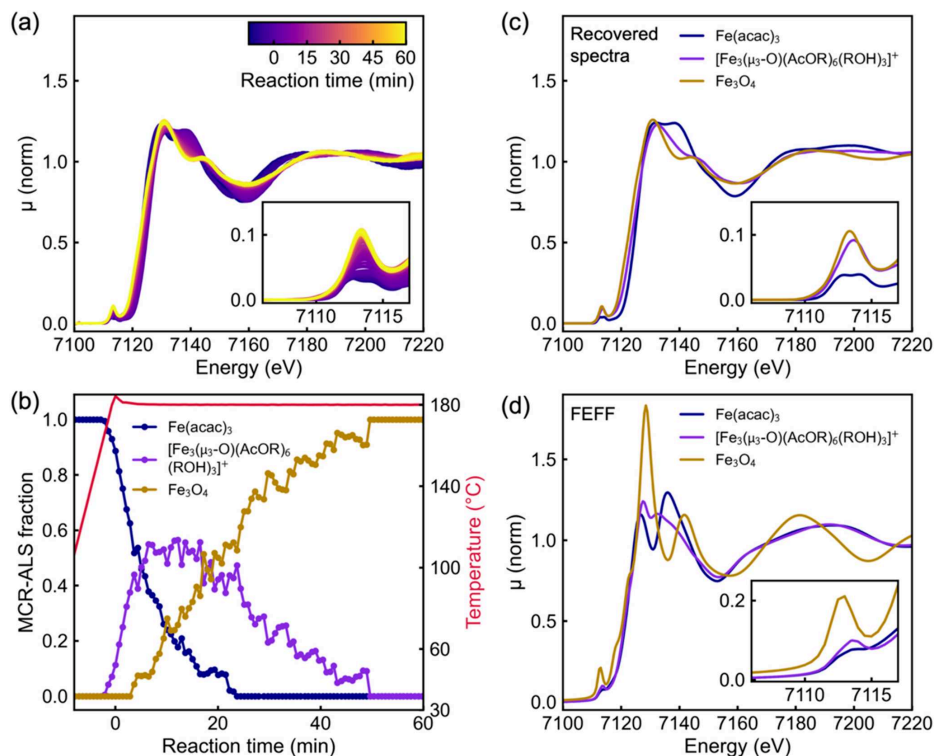


Figure 5

*In situ* ATR-FTIR analysis of the reaction of  $\text{Fe}(\text{acac})_3$  to  $\text{Fe}_3\text{O}_4$  in BnOH, compared with reference spectra of acetone and benzyl acetate,  $\text{Fe}(\text{acac})_3$  dissolved in BnOH at room temperature, and BnOH at  $180^\circ\text{C}$ .


**Figure 6**

*In situ* Fe K-edge HERFD-XANES analysis of the reaction to  $\text{Fe}_3\text{O}_4$ . (a) *In situ* HERFD-XANES data. (b) Concentration profiles of three distinct Fe species extracted via MCR-ALS. (c) MCR-ALS recovered spectra. (d) FEFF simulations based on structures determined from *in situ* PDF analysis, confirming the initial species as  $\text{Fe}(\text{acac})_3$ , the intermediate as  $[\text{Fe}_3(\mu_3\text{-O})(\text{AcOR})_6(\text{ROH})_3]^+$  and  $\text{Fe}_3\text{O}_4$  as the final product.

of solvothermal reactions. The reactor supports techniques such as XAS, WAXS and SAXS under inert, autoclave-like conditions. Its modular design features exchangeable inlets tailored to specific experimental requirements: PEEK for X-ray spectroscopy, and glass inlets for X-ray scattering. Additional configurations enable gas or liquid injection and integration of an ATR-IR fiber probe for simultaneous ATR-FTIR measurements. The reactor enables precise temperature control ( $-20^\circ\text{C}$  to  $200^\circ\text{C}$ ) with cartridge heaters or Peltier elements and magnetic stirring. The compact geometry is compatible with synchrotron beamline constraints and supports data acquisition in both transmission and reflection geometries.

We demonstrate the reactor's performance by investigating the synthesis of  $\text{Fe}_3\text{O}_4$  nanoparticles from  $\text{Fe}(\text{acac})_3$  in benzyl alcohol, as shown in Fig. 7. By linking findings from *in situ* PXRD, PDF of TS, HERFD-XANES, and ATR-FTIR, we comprehensively study the reaction pathways and reveal ferric acetate as an intermediate structure. This study underlines the potential of our reactor platform to provide mechanistic insights into solvothermal reactions and nanoparticle formation processes in real time, paving the way for rational synthesis design.

## 5. Experimental section

### 5.1. Chemicals

All chemicals were purchased from commercial sources and used without further purification:  $\text{Fe}(\text{acac})_3$  (Sigma Aldrich,

99.9%), benzyl alcohol (Sigma Aldrich, 99.8%), copper(II) oxide (Sigma Aldrich, 99.999%), ethanol (VWR Chemicals, >99.9%).  $\text{Fe}(\text{acac})_3$  and benzyl alcohol were stored and handled in the glove box under an inert atmosphere [ $\text{Ar}$  6.0 purity,  $c(\text{H}_2\text{O}) < 0.1$  p.p.m.,  $c(\text{O}_2) < 0.1$  p.p.m.].

### 5.2. Synthesis

In a typical synthesis, a stock solution was prepared in the glove box by adding  $\text{Fe}(\text{acac})_3$  (353.2 mg, 1.0 mmol) to 5 ml of benzyl alcohol and stirring until the iron salt was completely dissolved. Subsequently, a quantity of 80  $\mu\text{l}$  was transferred to the inlet of the reactor. After assembling the reactor, it was taken out of the glove box and heated to  $180^\circ\text{C}$  with a heating rate of  $10^\circ\text{C min}^{-1}$  under vigorous stirring. After the desired reaction time at  $180^\circ\text{C}$  the reactor was cooled to room temperature.

### 5.3. X-ray transmission calculations

X-ray transmission was calculated by first determining the X-ray absorption coefficients of the respective materials using the *Xraydb* Python library (Elam *et al.*, 2002; Newville, 2025) and applying Lambert's law to compute the transmission.

### 5.4. Attenuated total reflection Fourier transformed infrared (ATR-FTIR) spectroscopy

A ThermoFisher Nicolet iS20 equipped with a liquid  $\text{N}_2$ -cooled mercury-cadmium-telluride (MCT) detector, combined with a 6.3 mm high-temperature diamond ATR

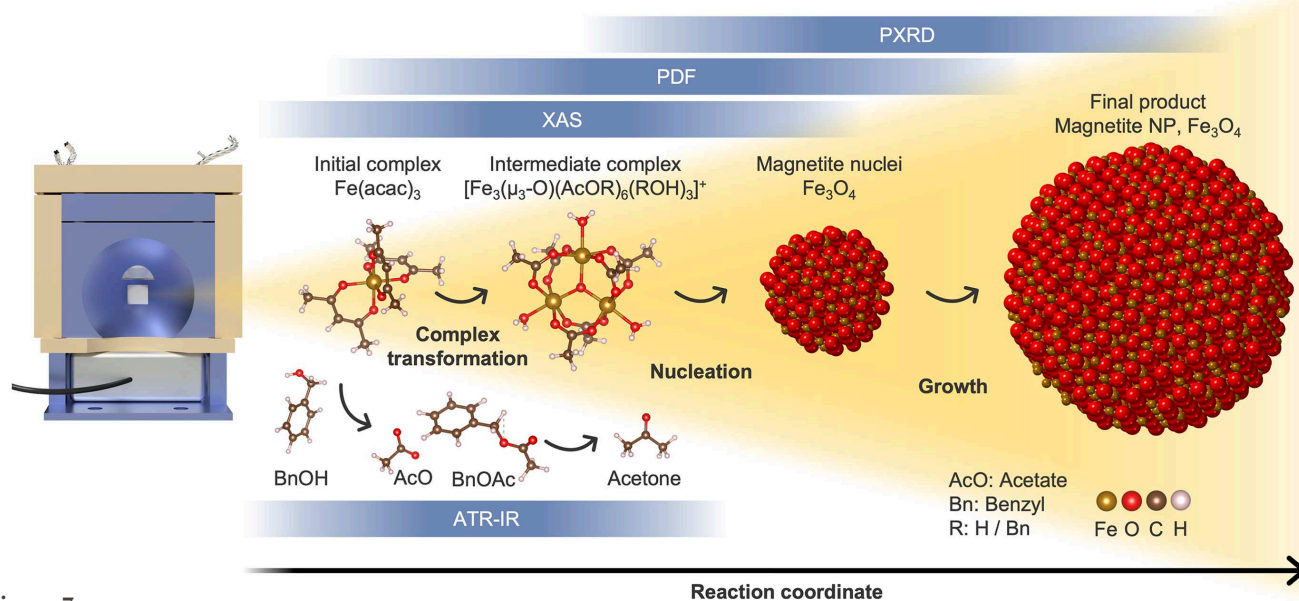


**Figure 7**

Schematic overview of the reaction pathway leading to magnetite ( $\text{Fe}_3\text{O}_4$ ) nanoparticles (NPs). The mechanism is elucidated using a combination of *in situ* techniques made possible by the versatile reactor setup. ATR-IR spectroscopy monitors the evolution of organic species throughout the reaction. XAS and PDF analyses reveal the conversion of the initial iron(III) acetylacetonate complex to the intermediate ferric acetate complex, followed by the formation of the magnetite phase. PXRD measurements track the emergence of the magnetite crystal structure and NP growth.

probe (art photonics, Berlin, Germany) was used for *in situ* ATR-IR measurements. Difference spectra were acquired using 32 scans and a spectral resolution of  $4\text{ cm}^{-1}$ , resulting in a time resolution of 48 s. To minimize thermal effects on the absorbance, a background of benzyl alcohol preheated to  $180^\circ\text{C}$  was used for the *in situ* analytical experiments. Spectra of reference compounds were acquired in absolute mode with a background of fiber in air.

### 5.5. *in situ* High-energy-resolution fluorescence-detected X-ray absorption near-edge structure (HERFD-XANES)

The *in situ* HERFD-XAS was measured in the PEEK inlet with 0.2 mm wall thickness. The data were acquired at the ID26 beamline (Gauthier *et al.*, 1999) at the European Synchrotron Radiation Facility (ESRF) in Grenoble, France. HERFD-XAS measurements were performed by measuring the intensity of the Fe  $K\alpha$  main line using a Ge(440) crystal in Rowland geometry (Glatzel *et al.*, 2021) while scanning the incident energy across the range of 7.10 to 7.22 keV with a step size of 0.1 eV. A Si(111) monochromator was used, and the overall energy resolution was  $\sim 1.4$  eV. To minimize radiation damage, the incident X-ray beam spot is moved onto the reaction cell after each scan, as shown in Figs. S12 and S13. Each HERFD-XAS spectrum was collected over 35 s.

The HERFD-XAS datasets were processed utilizing a custom Python script. The absorption-edge position was determined, and the edge jump was normalized using the *LARCH-XAFS* software module (Newville, 2013). Spectroscopic data underwent smoothing via a Savitzky–Golay filter and additional processing with the *NumPy* and *SciPy* libraries. A comparison between the raw and processed data is depicted in Fig. S14.

### 5.6. *in situ* Pair distribution function (PDF) analysis of *in situ* total scattering (TS) and powder X-ray diffraction (PXRD)

*In situ* TS and PXRD were measured in the glass inlet with 0.3 mm wall thickness. The data were acquired at beamline P21.1 at PETRA III at Deutsches Elektronen-Synchrotron DESY, Hamburg, Germany (von Zimmermann *et al.*, 2025). Two-dimensional scattering patterns were recorded every 1 s at an X-ray energy of 101.39 keV ( $\lambda = 0.1222\text{ \AA}$ ) using an X-ray area detector (PerkinElmer XRD1621, Varex Imaging Corp.) with  $2048 \times 2048$  pixels and a pixel size of  $200\text{ }\mu\text{m} \times 200\text{ }\mu\text{m}$ . An  $\text{LaB}_6$  powder standard packed into the fused silica inlet of the *in situ* reactor was used to calibrate the sample-to-detector distance: 0.390 m for *in situ* TS measurements of  $\text{Fe}_3\text{O}_4$  synthesis and 1.541 m for *ex situ* PXRD of CuO. For the TS data,  $q_{\text{damp}}$  and  $q_{\text{broad}}$  values were calibrated as  $0.0494\text{ \AA}^{-1}$  and  $0.0374\text{ \AA}^{-1}$ , respectively. PDF data were processed with  $q_{\text{min}} = 1.1\text{ \AA}^{-1}$ ,  $q_{\text{max}} = 14.2\text{ \AA}^{-1}$ ,  $q_{\text{max,inst}} = 24.0\text{ \AA}^{-1}$ , and  $r_{\text{poly}} = 0.9$ . Azimuthal integration and calibration were carried out using *pyFAI* (Kieffer & Wright, 2013), and PDF refinements were performed using *diffrpy-CMI* (Juhás *et al.*, 2015). Rietveld refinements were conducted with *GSAS-II* (Toby & Von Dreele, 2013). A detailed description of the data processing and PDF analysis procedures is available in the literature (Harouna-Mayer *et al.*, 2025).

### Acknowledgements

The authors acknowledge DESY (Hamburg, Germany), a member of the Helmholtz Association, and ESRF (Grenoble, France) for the provision of experimental facilities. Parts of this research were carried out at PETRA III using beamline

P21.1 (von Zimmermann *et al.*, 2025) and at ESRF using beamline ID26 under proposal MA5366 (Belgardt *et al.*, 2024). The authors also thank the beamline staff for their support with the experiments: at ID26, Dr Pieter Glatzel; at P21.1, Dr Martin v. Zimmermann, Dr Fernando Igoa, Dr Jiayu Liu, Philipp Glaeveccke and Olof Gutowski. Further, the authors thank Stefan Fleig and the workshop team at the University of Hamburg for machining the custom reactor components. We acknowledge financial support from the Open Access Publication Fund of Universität Hamburg. Open access funding enabled and organized by Projekt DEAL.

### Conflict of interest

The authors declare that there are no conflicts of interest.

### Data availability

All data presented in this report and three-dimensional step-files of the *in situ* reactor are available at <https://dx.doi.org/10.25592/uhhfdm.17624>. A self-written Python script for operating the LS335 temperature controller is available at <https://gitlab.rz.uni-hamburg.de/koziej-lab/in-situ-cell>.

### Funding information

This research was supported by the European Research Council (LINCHPIN project, grant No. 818941), the Deutsche Forschungsgemeinschaft (DFG) through the Cluster of Excellence ‘Advanced Imaging of Matter’ (EXC 2056, project ID 390715994) and by the Bundesministerium für Bildung und Forschung (BMBF) via the project 05K22GU7 (LUCENT II) and the project 05-K2020-2019-06104 XStereoVision (grant No. 05K20GUA).

### References

Andersen, C. W., Borfecchia, E., Bremholm, M., Jørgensen, M. R. V., Vennestrøm, P. N. R., Lamberti, C., Lundegaard, L. F. & Iversen, B. B. (2017). *Angew. Chem. Int. Ed.* **56**, 10367–10372.

Anson, C. E., Bourke, J. P., Cannon, R. D., Jayasooriya, U. A., Molinier, M. & Powell, A. K. (1997). *Inorg. Chem.* **36**, 1265–1267.

Bare, S. R., Yang, N., Kelly, S. D., Mickelson, G. E. & Modica, F. S. (2007). *Catal. Today* **126**, 18–26.

Bauer, M., Kauf, T., Christoffers, J. & Bertagnolli, H. (2005). *Phys. Chem. Chem. Phys.* **7**, 2664.

Becker, J., Bremholm, M., Tyrsted, C., Pauw, B., Jensen, K. M. Ø., Eltzholt, J., Christensen, M. & Iversen, B. B. (2010). *J. Appl. Cryst.* **43**, 729–736.

Belgardt, L., Grone, T. L. R., Hsu, C., Klemeyer, L., Koziej, D. & Zito, C. (2024). *In situ photon-in-photon-out spectroscopic studies with high temporal, spatial and energy resolution during emergence of transition metal su* [Dataset]. European Synchrotron Radiation Facility. Available at: <https://doi.esrf.fr/10.15151/ESRF-ES-1470339106>.

Beyer, K. A., Zhao, H., Borkiewicz, O. J., Newton, M. A., Chupas, P. J. & Chapman, K. W. (2014). *J. Appl. Cryst.* **47**, 95–101.

Bøjesen, D. & Iversen, E. (2016). *CrystEngComm* **18**, 8332–8353.

Boles, M. A., Ling, D., Hyeon, T. & Talapin, D. V. (2016). *Nat. Mater.* **15**, 141–153.

Borkiewicz, O. J., Shyam, B., Wiaderek, K. M., Kurtz, C., Chupas, P. J. & Chapman, K. W. (2012). *J. Appl. Cryst.* **45**, 1261–1269.

Broge, N. L. N., Søndergaard-Pedersen, F., Roelsgaard, M., Hassing-Hansen, X. & Iversen, B. B. (2020). *Nanoscale* **12**, 8511–8518.

Cansell, F. & Aymonier, C. (2009). *J. Supercrit. Fluids* **47**, 508–516.

Chupas, P. J., Chapman, K. W., Kurtz, C., Hanson, J. C., Lee, P. L. & Grey, C. P. (2008). *J. Appl. Cryst.* **41**, 822–824.

Derelli, D., Frank, K., Grote, L., Mancini, F., Dippel, A., Gutowski, O., Nickel, B. & Koziej, D. (2024). *Small* **20**, 2311714.

Deshmukh, R. & Niederberger, M. (2017). *Chem. Eur. J.* **23**, 8542–8570.

Elam, W. T., Ravel, B. D. & Sieber, J. R. (2002). *Radiat. Phys. Chem.* **63**, 121–128.

Evans, J. S. O., Francis, R. J., O’Hare, D., Price, S. J., Clark, S. M., Flaherty, J., Gordon, J., Nield, A. & Tang, C. C. (1995). *Rev. Sci. Instrum.* **66**, 2442–2445.

Fantechi, E., Roca, A. G., Sepúlveda, B., Torruella, P., Estradé, S., Peiró, F., Coy, E., Jurga, S., Bastús, N. G., Nogués, J. & Puntès, V. (2017). *Chem. Mater.* **29**, 4022–4035.

Fingland, B. R., Ribeiro, F. H. & Miller, J. T. (2009). *Catal. Lett.* **131**, 1–6.

Gauthier, C., Solé, V. A., Signorato, R., Goulon, J. & Moguiline, E. (1999). *J. Synchrotron Rad.* **6**, 164–166.

Glatzel, P., Harris, A., Marion, P., Sikora, M., Weng, T.-C., Guilloud, C., Lafuerza, S., Rovezzi, M., Detlefs, B. & Ducotté, L. (2021). *J. Synchrotron Rad.* **28**, 362–371.

Grosso, D., Boissière, C., Smarsly, B., Brezesinski, T., Pinna, N., Albouy, P. A., Amenitsch, H., Antonietti, M. & Sanchez, C. (2004). *Nat. Mater.* **3**, 787–792.

Grote, L., Zito, C. A., Frank, K., Dippel, A. C., Reisbeck, P., Pitala, K., Kvashnina, K. O., Bauters, S., Detlefs, B., Ivashko, O., Pandit, P., Rebber, M., Harouna-Mayer, S. Y., Nickel, B. & Koziej, D. (2021). *Nat. Commun.* **12**, 4429.

Grunwaldt, J.-D., Ramin, M., Rohr, M., Michailovski, A., Patzke, G. R. & Baiker, A. (2005). *Rev. Sci. Instrum.* **76**, 054104.

Harouna-Mayer, S. Y., Kopula Kesavan, J., Caddeo, F., Belgardt, L., Hsu, C., Klemeyer, L., Kipping, L., Akcaalan, M. G., Groene, T. R. L., Köppen, A., Noei, H., Mathon, O., Dippel, A. & Koziej, D. (2025). *Small* **21**, e2506838.

Heidenreich, N., Rütt, U., Köppen, M., Inge, A. K., Beier, S., Dippel, A. C., Suren, R. & Stock, N. (2017). *Rev. Sci. Instrum.* **88**, 104102.

Heiligtag, F. J. & Niederberger, M. (2013). *Mater. Today* **16**, 262–271.

Hoffman, A. S., Singh, J. A., Bent, S. F. & Bare, S. R. (2018). *J. Synchrotron Rad.* **25**, 1673–1682.

Jaumot, J., Gargallo, R., de Juan, A. & Tauler, R. (2005). *Chemom. Intell. Lab. Syst.* **76**, 101–110.

Jensen, K. M. Ø., Tyrsted, C., Bremholm, M. & Iversen, B. B. (2014). *ChemSusChem* **7**, 1594–1611.

Juhás, P., Farrow, C., Yang, X., Knox, K. & Billinge, S. (2015). *Acta Cryst.* **A71**, 562–568.

Kalantzopoulos, G. N., Lundvall, F., Checchia, S., Lind, A., Wragg, D. S., Fjellvåg, H. & Arstad, B. (2018). *ChemPhysChem* **19**, 519–528.

Kieffer, J. & Wright, J. P. (2013). *Powder Diffr.* **28**, S339–S350.

Kim, D., Lee, N., Park, M., Kim, B. H., An, K. & Hyeon, T. (2009). *J. Am. Chem. Soc.* **131**, 454–455.

Klemeyer, L., Caddeo, F., Gröne, T. L. R., Harouna-Mayer, S. Y., Jessen, B., Zito, C. A., Kopula Kesavan, J., Dippel, A. C., Igoa Saldaña, F., Mathon, O., Glatzel, P. & Koziej, D. (2025). *ACS Nano* **19**, 25710–25719.

Klemeyer, L., Gröne, T. L. R., Zito, C. A., Vasylieva, O., Gumus Akcaalan, M., Harouna-Mayer, S. Y., Caddeo, F., Steenbock, T., Hussak, S., Kesavan, J. K., Dippel, A., Sun, X., Köppen, A., Saveleva, V. A., Kumar, S., Bester, G., Glatzel, P. & Koziej, D. (2024). *J. Am. Chem. Soc.* **146**, 33475–33484.

Koziej, D. (2016). *Chem. Mater.* **28**, 2478–2490.

Levish, A. & Winterer, M. (2020). *Rev. Sci. Instrum.* **91**, 063101.

- Mikhailova, M. A., Chernyshov, I. Y., Illarionov, G. A., Kolchanov, D. S., Kuchur, O. A., Vinogradov, A. V., Morozova, S. M. & Morozov, M. I. (2022). *J. Mater. Chem. C* **10**, 251–264.
- Newville, M. (2013). *J. Phys. Conf. Ser.* **430**, 012007.
- Newville, M. (2025). *xraypy/XrayDB*, <https://github.com/xraypy/XrayDB>.
- Niederberger, M. & Garnweitner, G. (2006). *Chem. Eur. J.* **12**, 7282–7302.
- Nobile, C. & Cozzoli, P. D. (2022). *Nanomaterials* **12**, 1729.
- Okudera, H., Yoshiasa, A., Murai, K., Okube, M., Takeda, T. & Kikkawa, S. (2012). *J. Mineral. Petrol. Sci.* **107**, 127–132.
- Onur Şahin, E., Tüysüz, H., Chan, C. K., Moon, G., Dai, Y., Schmidt, W., Lim, J., Scheu, C. & Weidenthaler, C. (2021). *Nanoscale* **13**, 150–162.
- Pinna, N., Grancharov, S., Beato, P., Bonville, P., Antonietti, M. & Niederberger, M. (2005). *Chem. Mater.* **17**, 3044–3049.
- Piquer, C., Laguna-Marco, M. A., Roca, A. G., Boada, R., Guglieri, C. & Chaboy, J. (2014). *J. Phys. Chem. C* **118**, 1332–1346.
- Prinz, N., Strübbe, S., Bauer, M. & Zobel, M. (2023). *New J. Chem.* **47**, 11623–11635.
- Rehr, J. J., Kas, J. J., Vila, F. D., Prange, M. P. & Jorissen, K. (2010). *Phys. Chem. Chem. Phys.* **12**, 5503–5513.
- Roelsgaard, M., Kløve, M., Christensen, R., Bertelsen, A. D., Broge, N. L. N., Kantor, I., Sørensen, D. R., Dippel, A.-C., Banerjee, S., Zimmermann, M. V., Glaevecke, P., Gutowski, O., Jørgensen, M. R. V. & Iversen, B. B. (2023). *J. Appl. Cryst.* **56**, 581–588.
- Schäef, H. T., Windisch, C. F. Jr., McGrail, B. P., Martin, P. F. & Rosso, K. M. (2011). *Geochim. Cosmochim. Acta.* **75**, 7458–7471.
- Staniuk, M., Hirsch, O., Kränzlin, N., Böhlen, R., van Beek, W., Abdala, P. M. & Koziej, D. (2014). *Chem. Mater.* **26**, 2086–2094.
- Terraschke, H. (2023). *Nanostructured materials: applications, synthesis and in-situ characterization*. Walter de Gruyter GmbH & Co KG.
- Testemale, D. & Brugger, J. (2024). *International tables for crystallography*, Vol. I, ch. 3.25, pp. 461–465. International Union of Crystallography.
- Testemale, D., Pokrovski, G. S., Lahera, E., Prat, A., Kieffer, I., Delnet, W., Proux, O., Louvel, M., Sanchez-Valle, C. & Hazemann, J. L. (2024). *High Pressure Res.* **44**, 277–293.
- Thum, L., Arzmann, M., Zizak, I., Grüneberger, R., Steigert, A., Grimm, N., Wallacher, D., Schlatmann, R., Amkreutz, D. & Gili, A. (2024). *Rev. Sci. Instrum.* **95**, 033904.
- Toby, B. H. & Von Dreele, R. B. (2013). *J. Appl. Cryst.* **46**, 544–549.
- Tominaka, S., Yamada, H., Hiroi, S., Kawaguchi, S. I. & Ohara, K. (2018). *ACS Omega* **3**, 8874–8881.
- van Beek, W., Safonova, O. V., Wiker, G. & Emerich, H. (2011). *Phase Transit.* **84**, 726–732.
- Wang, H., Mo, G., Zhong, J., Liu, Y., Qian, L., Yao, L., Xing, X., Chen, Z. & Wu, Z. (2022). *Nucl. Instrum. Methods Phys. Res. A* **1031**, 166605.
- Yamada, H., Tominaka, S., Ohara, K., Liu, Z., Okubo, T. & Wakihara, T. (2019). *J. Phys. Chem. C* **123**, 28419–28426.
- Yao, S., Yang, C., Zhao, H., Li, S., Lin, L., Wen, W., Liu, J., Hu, G., Li, W., Hou, Y. & Ma, D. (2017). *J. Phys. Chem. C* **121**, 5154–5160.
- Yi, Z., Dumée, L. F., Garvey, C. J., Feng, C., She, F., Rookes, J. E., Mudie, S., Cahill, D. M. & Kong, L. (2015). *Langmuir* **31**, 8478–8487.
- Yin, Y. & Talapin, D. (2013). *Chem. Soc. Rev.* **42**, 2484–2487.
- Zhu, H., Huang, Y., Ren, J., Zhang, B., Ke, Y., Jen, A. K., Zhang, Q., Wang, X. & Liu, Q. (2021). *Adv. Sci.* **8**, 2003534.
- Zimmermann, M., v. Ivashko, O., Igoa Saldaña, F., Liu, J., Glaevecke, P., Gutowski, O., Nowak, R., Köhler, K., Winkler, B., Schöps, A., Schulte-Schrepping, H. & Dippel, A.-C. (2025). *J. Synchrotron Rad.* **32**, 802–814.